Uniaxial force modifies the length of the mammary ductal network and the orientation of ducts during pubertal development: Findings from computational modeling and laboratory experiments

Daisy Ulloa [1,2], Uduak Z George [1,2*]

1 Department of Mathematics and Statistics, San Diego State University, San Diego, California, USA

2 Computational Science Research Center, San Diego State University, San Diego, California, USA

3 Department of Animal Sciences, Purdue University, West Lafayette, Indiana, USA

* corresponding author (ugeorge@sdsu.edu)

Abstract

Mammary gland forms an extensive tree-like network of epithelium ducts during puberty. The orientation of the epithelium ducts determine the overall shape of the epithelium ductal network which in turn impacts the delivery of milk through the ducts to breastfeeding infants. However, how the orientation of the ducts are specified is not well understood. This study examines if an applied force can regulate the orientation of the epithelium ducts during puberty, in vivo. Exogenous forces were applied continuously to pairs of abdominal number four mammary glands in mice, during pubertal formation of the epithelium ductal network at 5-7 weeks of age. In each mice (n=10), one of the abdominal number four mammary gland was exposed to a uniaxial force (TEN) and the other was exposed to a contralateral (CONTRA) force. Subsequently, microscopy images of the epithelium ductal network for the TEN and CONTRA glands were analyzed and compared to controls to determine differences in ductal orientation. Findings from image-based analysis indicate that uniaxial and contralateral forces increase the length of the ductal network. Though the ductal network were longer in the TEN and CONTRA glands, there were no significant differences in the total cross-sectional area of the ductal network compared to controls. However, the orientation of the epithelium ducts in TEN and CONTRA glands were different compared to controls. In-silico simulations of ductal network formation with a branching and annihilating random walk model predicts that the orientation of the epithelium ducts may significantly alter the length of the ductal network. These findings suggest that the increased

length of the ductal network resulted from the changes in the orientation of the epithelium ducts. This study therefore determines that exogeneous mechanical forces may regulate ductal network architecture and orientation of ductal branches in vivo.

1 Introduction

Tissue mechanical environment plays a major role in the proper formation of epithelium and glandular tissues with tree-like structures, such as the lung airways, the salivary gland, pancreas ducts, and the mammary epithelium ducts [1]. These tree-like structures are critical for long-term physiological functioning of the body and developmental defects often lead to poor health outcomes [2–6]. The female mammary gland is a great model for studying branching morphogenesis because the development of its epithelial ductal network occurs postnatally during puberty, allowing for investigations into the evolution of these complex network structures after birth, in vivo. Though it is known that mechanical forces affect branching morphogenesis (a process that governs the formation of tree-like tissues) in the mammary gland, its effect is not fully understood nor well characterized. How the orientation of the epithelium ductal branches is specified remains an open question [1, 7–9]. A crucial step for elucidating how the orientations of epithelial ductal branches are specified involve identifying mechanisms that modulate or regulate branch orientation. This is vital because it would facilitate the selection of potential regulatory candidates and enable the formulation of hypotheses that can be tested through laboratory experiments and/or computational modeling. Therefore, in this study, we perturbed the mechanical environment and examined how it modifes the orientation of the epithelium ducts in the mammary gland, in vivo.

During puberty, an extensive network of epithelium ducts emerges from a rudimentary ductal structure via the process of branching morphogenesis (Fig. 1A, [10, 11]). In the mammary gland, branching morphogenesis occurs via two main stages: the first stage is through successive rounds of elongation and splitting of the tips of existing/parent ducts (i.e., tip bifurcation) and the second stage is through the elongation of buds that protrude along the sides of existing ducts (i.e, side branching) [12]. Majority of the studies on mammary ductal network formation have focused on identifying the molecular factors that regulate the development of the ductal network including ductal elongation, tip bifurcation, and side branching [13–22]. However, comparatively fewer studies focus on deciphering the role of mechanical forces in mammary ductal network formation. Existing research on the effects of tissue mechanics on ductal network formation highlights a significant need for further investigation [23, 24].

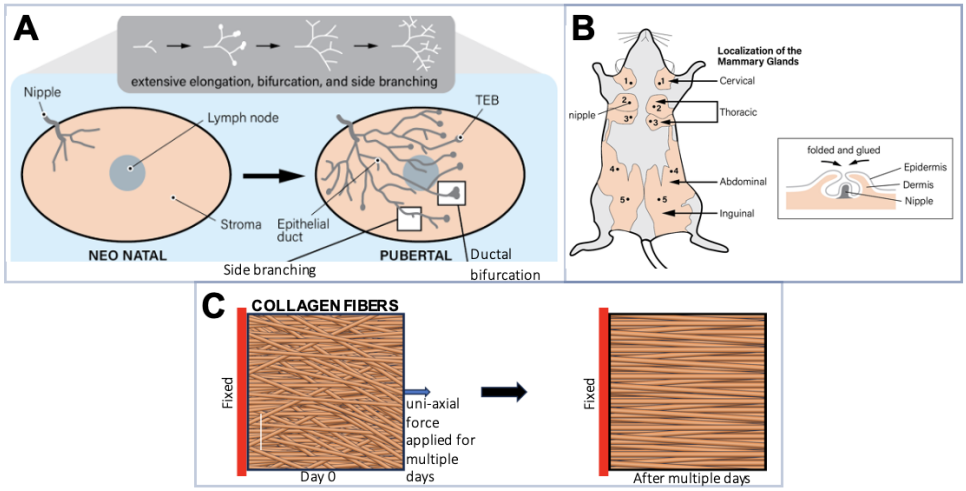

Fig 1. Overview of pubertal branching morphogenesis and laboratory experimentation. (A) Neonatal versus pubertal mammary gland. The formation of an extensive network of epithelium ducts occurs during pubertal development via ductal elongation, tip bifurcation and side branching. (B) The right abdominal number four mammary gland was used to investigate the role of tensional force on mouse branching morphogenesis. The inset shows how a uniaxial tension force was applied to the right abdominal number four mammary gland. The skin surrounding the nipple was lifted, folded and glued together as shown. (C) Schematics showing collagen reorientation after continuous application of a uniaxial force/strain.

Observations of branching morphogenesis in organoid models demonstrate that the mechanical properties of the region around the ductal branch can regulate the global pattern of the mammary epithelium network [23, 24]. However, organoids are not capable of accurately modeling the complexity of the in vivo mammary gland environment, therefore in vivo studies are needed for investigating the role of mechanical forces in the formation of the ductal network. Therefore, in this study, we aimed to determine whether mechanical forces, applied in vivo, can regulate the orientations of the epithelium ductal branches and the overall ductal network architecture.

We applied a uniaxial force to the right abdominal number four mammary gland in mice for two-weeks during pubertal development to determine if mechanical forces can regulate the orientation of the ductal branches (Fig. 1B, inset). By applying a uniaxial force to the mammary gland, we are changing the mechanical environment in the stroma, a key tissue component in the mammary gland (Fig. 1A, [25–27]). de Jonge et al [28] studied collagen reorganization in fibrin based engineered tissues under uniaxial strain applied continuously for 12 days. By analyzing time-lapse images of collagen orientation, they found that collagen orientation changed gradually from random orientation at day 0 to being parallel to the direction of the uniaxial strain by day 4. Based on this, we believe that the application of a continuous uniaxial strain to the mammary gland can change collagen organization and orients the collagen fibers towards the direction of the applied force (Fig. 1C). Though complete

alignment of collagen may be obtained after multiple days of applying a uniaxial force, we believe that the degree of alignment of the collagen fibers to the direction of the uniaxial strain would also depend on the magnitude of the applied force. Therefore, by applying a uniaxial force to the mammary gland, we are potentially influencing cell-signaling and the ductal branching process. Collagen fibers alignment can significantly influence the overall stiffness of the stroma because when collagen fibers are aligned parallel to the direction of an applied load or stress, the tissue exhibits increased stiffness and tensile strength along that direction. Conversely, when collagen fibers are randomly oriented or misaligned, the tissue may exhibit lower stiffness and mechanical integrity. Cells sense the stiffness of the stroma and respond through the process of mechanotransduction. Mechanical signaling can lead to functional and/or structural responses in the cells and tissues by influencing cell adhesion, migration, morphology and differentiation [29, 30], which are key processes involved in branching morphogenesis [31].

We analyzed microscopy images of mammary glands subjected to uniaxial force and compared them to control samples to evaluate its effects on ductal network formation. Uniaxial force applied to the right abdominal number four mammary gland induced a contralateral force on the left abdominal number four mammary gland, resulting in unilateral pulling of the left gland, whereas the right gland experienced bilaterally directed pulling. We examined the morphology of the ductal network including the orientation of ductal branches, the length and width of the overall ductal network, the cross-sectional area of the epithelium network, number of perimetral branches in glands that experience uniaxial and contalateral forces and compared them to controls. We used a branching and annihilating random walk model to determine why the ductal network in the mammary glands exposed to uniaxial and contralateral forces where longer than those in controls. Findings from this study indicates that mechanical forces may regulate the ductal network architecture by modifying the orientation of ductal branches and the overall length of the ductal networks. This study contributes to increasing our understanding of the effect of mechanical forces on the formation of epithelium ductal networks.

2 Materials and methods

2.1 Laboratory experimentation: Application of a uniaxial tension force to the mammary gland

Prior to initiating this study, the protocols were reviewed and approved by Purdue University's Institutional Animal Care and Use Committee (protocol #190100845). Mice (n=32) used in this study were offspring born to Wap-cre (B6129-Tg(Wap-cre)11738Mam/J) and wild type C57BL/6J crosses

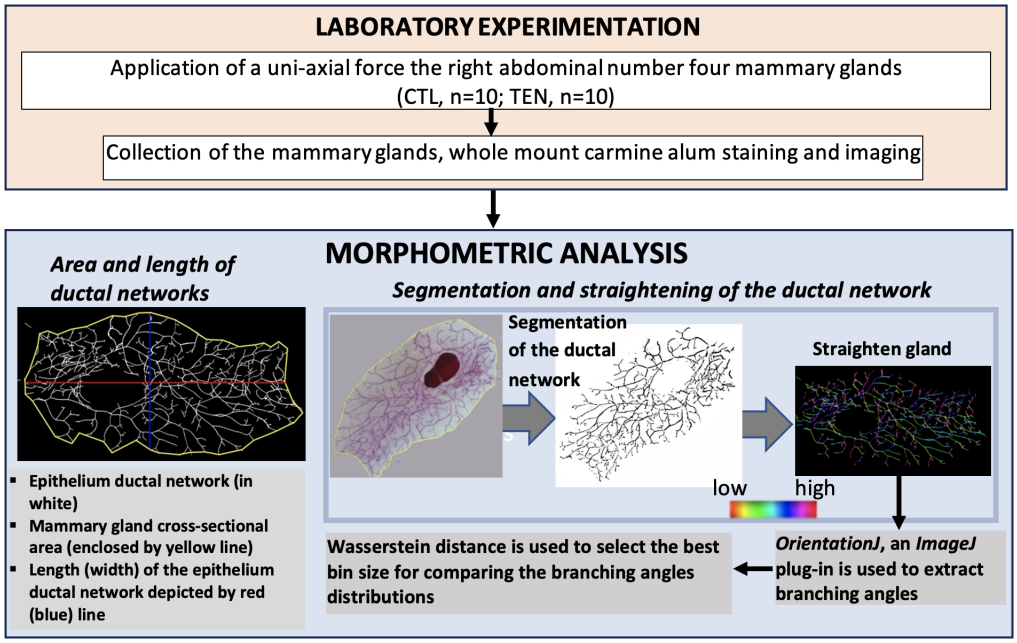

Fig 2. Study design for experimentation and morphometric analysis. The color map shows high and low branching angles. Morphometrics was obtained for all of the CTL, TEN and CONTRA glands.

(Jackson Laboratory, Bar Harbor, ME) bred in the Casey laboratory at Purdue University. Genotypes of offspring produced by this cross are either wild type or heterozygous Wap-cre. Heterozygous Wap-cre offspring do not show an overt phenotype and animals were not genotyped for this study. Female offspring were euthanized via CO2 inhalation at 3 weeks of age (n=6) and at 5 weeks of age (n=6) and their mammary glands were inspected visually in order to confirm that the mammary glands were undergoing normal development and the stage of development was consistent with the age of the mice. The remaining female offspring (n=20) were randomly assigned to one of two groups: control (CTL, n=10) and experimental group (n=10). At five weeks of age, the female mice were anesthetized using 3% isoflurane gas with a flow rate of 1.0 L/minute oxygen. The fur surrounding the nipple of the right abdominal number four mammary gland was removed by plucking with a forcep. The skin on either side of the right nipple was lifted and glued together using topical tissue adhesive (GLUture, Zoetis In., Kalamazoo, MI, USA) to encase the nipple (Fig. 1B), exerting a uniaxial force on the mammary gland. These glands were referred to as TEN glands (n=10). The glue was checked daily. If glue was removed, the mice was anesthetized and skin was lifted and glued again. At 7 weeks of age, the mice in the experimental and control groups were euthanized and their mammary glands examined to determine the effect of the applied uni-axial and contralateral forces on the orientation and distribution of the epithelium ducts.

2.2 Collection of the mammary glands and whole mount carmine alum staining

Immediately after euthanasia, the right abdominal number four mammary glands were removed in both the CTL and TEN groups. Though the left abdominal four mammary glands in the TEN groups were not directly exposed to tensional forces, the gluing procedure pulls laterally on the skin beside its nipple thus indirectly exposing these glands to mechanical stress via contralateral forces. Therefore, the left abdominal four mammary glands were also extracted from mice in the TEN groups for analyzes and quantification of the effect of the contralateral forces on mammary gland branching morphogenesis. The extracted glands were placed on a plain frosted microscope slide (Fisher Scientific, Hampton, NJ, USA) and gently spread out with the blunt end of the forceps. After allowing the mammary whole mount to dry and adhere to the microscope slide for about 5 minutes, the slides were placed in Carnoy's solution (75% absolute ethanol and 25% glacial acetic acid) to fix overnight. The next day, the slides were transferred into carmine alum (Stemcell Technologies Inc., Vancouver, British Columbia, CA) and incubated overnight. The following day, slides were moved into destaining solution (70% absolute ethanol, 5.64% 37% HCl, and double distilled water) for 2 h. Next, slides were dehydrated in increasing concentrations of ethanol (70%, 80%, 95%, and 100%) for 30 minutes at a time. Lastly, slides were defatted in toluene for 30 min or until the fat is sufficiently cleared from the glands. A cover slip was applied using DPX mountant (Sigma-Aldrich, Burlington, MA, USA) and dried overnight. Once the whole mount carmine alum slides finished drying, slides were viewed with a M60 stereo microscope with a camera port (Leica Microsystems, Wetzlar, Germany). Images from the microscope were captured using a C-mount AmScope camera and saved using the AmScope software (AmScope, Irvine, CA, USA). Multiple images were taken to capture the entire gland by moving the slide across the span of the tissue. To create a single panorama image of the entire gland, Adobe Photoshop (V 23.0.1) was used to merge the individual images into a single image. The microscopy images of the entire mammary gland were used for morphometric analysis for CTL, TEN and CONTRA glands.

2.3 Morphometric analysis of the ductal network in the TEN, CONTRA and CTL glands

Morphometrics such as the area, length and global curvature of the ductal network and the orientation of the epithelium ducts where computed to determine differences between CTL, TEN and CONTRA glands (Fig. 2).

Curvature of the ductal network: The images of the entire mammary gland were used to compute the

global curvature of the ductal network in CTL, TEN and CONTRA glands. This was done using the Kappa Plugin in Fiji open source image processing package [32, 33]. Using the Kappa Plugin, we computed the average curvature, curve length, curvature, and point curvature.

Area and length of the ductal network: The total cross-sectional area of the ductal network for each gland was obtained using ImageJ version 1.54j [34] by thresholding the microscopy images to separate the epithelium ducts from the stroma (Fig. 2). After this was completed, the total pixel in the segmented epithelium ductal network was computed by using the Analyze Particles tool in ImageJ to determine the total cross-sectional area. A similar approach was used to calculate the total cross-sectional area of the whole mammary gland. Length of the long axis of the ductal network (Fig. 2) were taken using the Measure tool in ImageJ. We straighten the branched network to remove its global curvature and ensure that the long axis of the branched network is oriented along the x-axis [23]. This was done to ensure that we could accurately compare the length of ductal networks in TEN, CONTRA and CTL glands without bias from their global curvature. To straighten the branched network, we used the straighten tool in the edit menu in ImageJ. After we straighten the branched network, the Measure tool was used to measure the length of the straightened long axis of the ductal network from its originating point to the tip of the furthest branch along the long axis.

Orientations of the mammary ducts: The orientations of the mammary ducts were computed using OrientationJ version 16.01.2018 [23, 35–37], an ImageJ plug-in. In order to compute the orientations of the mammary ducts, the outline of the ductal network was manually traced out in Adobe Photoshop and the resulting skeletal outlines were straightened along the long axis using Fiji's Kappa plug [32]. Next we adjusted the ductal network so that the ends of ductal network in all the images pointed in the same direction, for consistency. Maintaining the consistency was important for establishing a common reference for computing and comparing ductal orientations between TEN, CONTRA and CTL glands. Finally, after adjusting the ductal networks to point in the same direction, we computed the orientation of the mammary ducts in the images for TEN, CONTRA and CTL glands. This was carried out using the *Analysis and Distribution* tool in OrientationJ. In the *Analysis and Distribution* tool, the variable local window σ was set to 10 pixels when computing the local orientations of the mammary ducts. The choice of the value of σ can significantly affect the resolution of the orientation analysis. The σ value specifies the size of the neighborhood around each pixel that is considered when computing the ductal orientation. σ was set to 10 pixels based on work from studies in the literature that demonstrate that this value of σ is adequate.

In OrientationJ, the minimum coherency and energy level was set to 0.1%, meaning pixels were detected if their levels were at or above this percent value. The angle distribution obtained from the

OrientationJ provided information on the number of pixels that where oriented in each integer degree value between $[-90, 90]$ (Fig. 2). This data provides a sum equal to the total pixels in an image, and the bar graphs generated for this data accurately describe the spatial variations in the orientation of the ducts. To find the proportion of branches that lie within a certain degree range, the sum of pixels in the chosen degree range was divided by the total number of pixels in the image. The proportion of ducts in each degree angle was used as a measure for the orientation of the ducts in the TEN, CONTRA, and CTL glands. We compared the distribution for the proportion of ducts in different angle ranges to determine differences between TEN, CONTRA and CTLs.

2.4 Optimal transport methodology for measuring similarities in ductal orientations (i.e. the branching angles distribution) between TEN, CONTRA and CTL glands

Optimal transport theory provides a measure to compute distances between pairs of probability distributions. This measure which is called Wasserstein distance $W(\mu, \eta)$ satisfy conditions that are desirable when comparing the similarities between two probability distributions say μ and η. One of the desirable condition is the symmetry condition $W(\mu, \eta) = W(\eta, \mu)$ [38]. Another desirable condition that $W(\mu, \eta)$ satisfies is $W(\mu, \eta) = 0$ if $\mu = \eta$, allowing us to measure similarities between the two probability distributions. Another commonly used metrics for computing the similarity between probability distributions is the Kullback–Leibler (KL) divergence. The KL divergence $D_{KL}(\mu||\eta)$ calculates a score that measures the divergence of the probability distribution μ from η defined on the same space ξ. If μ and η are discrete probability distributions, then $D_{KL}(\mu||\eta) = \sum_{x \in \xi} \left(\mu(x) \log \left(\frac{\mu(x)}{\eta(x)} \right) \right)$ [39]. A drawback of the KL divergence is that it does not satisfy the symmetry condition, that is $D_{KL}(\mu||\eta) \neq D_{KL}(\eta||\mu)$. That is, the divergence from distribution μ to η is not equal to the divergence from η to μ. Therefore, it is not a good approach for comparing similarities between our probability distributions and is often used as a measure of discrepancy between two distributions rather than a metric [39]. When measuring the similarities between the probability distributions for the branching angles between TENs vs. CTLs and CONTRAs vs. CTLs, we used the Wasserstein distance because it satisfies the symmetry condition.

Let μ represent the probability distribution for the branching angles for the TEN glands and η the branching angles for the CTL glands. The probability distribution μ (or η) is computed by calculating the proportion of branching angles of the TEN (or CTL) glands that lies between different ranges of angle. Therefore, the area under the curve of the probability density function (PDF) for μ and η are

equal and $W(\mu, \eta)$ computes the optimal cost of moving the contents of μ to obtain η. We represent the number of bins in μ and η by n. We denote the location of a bin in μ by x_i and the location for all the bins in μ as $\{x_i\}_{(i=1)}^{n}$. Similarly, we denote the location of the bins in η by $\{x_j\}_{(j=1)^n}$. The cost C_{ij} for moving one unit of item from bin i to bin j (or vice versa) is measured by the squared Euclidean distance:

$$C_{ij} = \|x_i - x_j\|, \tag{1}$$

where $C = (C_{ij})_{(1 \leq i, j \leq n)}$ is a symmetric matrix in $\mathbb{R}^{n \times n}$. We define a transportation plan $T \in \mathbb{R}^{n \times n}$, which tells us how many units of item to move from x_i to x_j. The total cost of a given transport plan is:

$$< T, C >= \sum_{i=1}^{n} \sum_{j=1}^{n} T_{ij} C_{ij},$$

And the optimal transport plan T^* is obtained by solving the following optimization problem:

$$\underset{\mathbf{T}}{\text{minimize}} \qquad \langle \mathbf{T}, \mathbf{C} \rangle \tag{2}$$

$$\text{subject to} \qquad \mathbf{T1} = \mathbf{p}, \quad \mathbf{T}^\top \mathbf{1} = \mathbf{q}, \quad \mathbf{T} \geq 0, \tag{3}$$

where $\mathbf{1}$ denotes a vector of ones. The Wasserstein distance is:

$$\mathcal{W}(\mu, \eta) = \left(\langle \mathbf{T}^*, \mathbf{C} \rangle \right)^{1/2},$$

and is used to measure the degree of similarity in branching angle distributions between TEN versus CTL glands and CONTRA versus CTL glands.

2.5 Modeling ductal network orientation with a biased branching and annihilating random walk model

We used a biased and annihilating random walk model to simulate ductal network formation and study how changes in the branch angles affect the morphology of the ductal network. The most simple random walk moves forward in space, where each step forward can move in a randomized direction. Random walk models can be described by two attributes: correlated/uncorrelated and biased/unbiased. Correlation refers to whether each step is based on the previous step; bias refers to whether each step has rules that influence direction [40]. Random walk models can be used to describe movement, such as Brownian motion, as well as cellular and molecular motion [40]. Hannezo et al [41] proposed

that correlated/persistent random walks can be used to describe the whole branching structure in the mammary gland. They used a simple rules of branching and annihilation (i.e. branch death), to create branching structures similar to those observed in experiments [41]. They were able to use the random walk model to investigate the number of branches that originate from another branch [42]. Random walks have also been used to investigate global bias along the epithelial orientation. To do so, Nerger et al [23] conducted a random walk simulation that controlled for branching angle between two bifurcating branches. The results concluded that a controlled bifurcation angle was able to reproduce the global bias in the epithelium observed in vivo. Their results predict bifurcation angle may dictate global orientation of the epithelium [23].

While the model proposed by Hannezo et al [41] predict epithelial branching using randomized steps with annihilation to describe branch growth and death [41], we introduce bias into our model to recreate results from the uniaxial tension force experiments. This bias in our model tends branching towards the specific angles that we observed to differentiate TEN, CONTRA, and CTLs in the laboratory experiments. The rules for the Hannezo et al model include a constant probability for bifurcation and death. Our model does include probabilities for bifurcation and death, however, we included another rule that forces a branch to bifurcate if the branch is too long. This was to ensure bifurcations would occur. The Hannezo et al model also tests bias in the distal direction at varying directional cues. Similar to Nerger et al [23], we controlled for the bifurcation angle, but at a broader range. Nerger et al controlled for bifurcation angles of approximately 75°, whereas we allowed for bifurcation angles from 30° - 90° to allow for bias in the movement.

An important distinction between the Hannezo et al [41] and our model is the introduction of bias to each step of the simulation by increasing the chance the step direction would occur at the bias value. However, the step direction was not always at the bias. The Hannezo et al model introduces bias at each step, and alters the angle towards the bias absolutely. To introduce bias, we use a function referred to as biased random value. This function works by picking an integer from a window centered about an angle α, and assigning weights to each integer in the window. The window ranges from [α + 15, α - 15] where each value in the window is divisible by 5. Values with a higher weight are more likely to be chosen whereas lower weights have less chance of being chosen. An example of the biased random value function is described as follows.

Biased random value function: (i) select Center = 10, bias value = 20; (ii) create a vector for window values [25 , 20 , 15, 10 , 5, 0 , -5] (iii) reorder values based on bias: [20, 25, 15, 10, 5, 0, -5] (iv) Assign weights to reordered list: [20%, 17%, 17%, 13%, 13%, 10%, 10%] where reordered window list at position i, is associated with weight at position i (v) uses Choices from Random package in Python

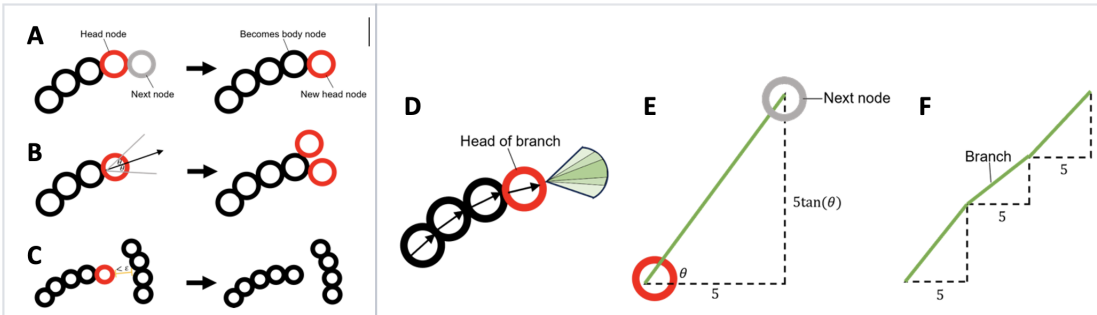

Fig 3. A Biased branching and annihilating random walk model. (A) Shows how head node property changes to a body node as a branch elongates or bifurcates. (B) shows how bifurcation occurs in the algorithm. (C) shows how the intersection functions detect other branches. The concept is the same for intersection of the boundary. (D) shows how the head node will choose the angle for the next node. (E) shows the placement of the next node based on the angle chosen in (D). (F) shows how the branch will form over several elongations

version 3.10.9 with reordered list and weights to choose a value.

Our model includes a set of rules for elongation, bifurcation, and intersection events. Each of these rules use a branch head node as input. The head node is defined as the most recent node of an alive branch that elongation, bifurcation, or death can occur from. Once an event has concluded, the head node will become a body node that is dormant (Fig. 3A). The rules also depend on information from a tracker array that holds the (x, y) coordinates of all body and head nodes. The intersection algorithms (Fig 3C) are a series of algorithms that check for intersections between the current head node and existing branches or the perimeter. The intersection algorithms have minute differences, but are functionally the same.

Intersection algorithm: (i) retrieve x,y coordinates of head node, (ii) search through tracker for x,y coordinates near head node, (iii) create bounding box of tracker coordinates, (iv) check if head node intersects with bounding box.

When the bifurcation event is triggered (Fig 3D), two new head nodes will be created from the current head node (Fig 3E). Two new angles are randomized, centered about the angle of the current head node. Then the elongation process is performed starting from the two new angles. The elongation process is described in more detail later.

Bifurcation algorithm: (i) use biased random value function to get value p, (ii) Retrieve current angle position of head node θ (iii) create two new head nodes with angle position $p + \theta$ and $p - \theta$, (iii) run elongation algorithm with new head nodes

The elongation algorithm is how the random walk function is performed. From the current head node, a step of size 5 in the x-direction is taken. The y-coordinate is determined by $5\tan(\theta)$ where θ is the angle of the next step (Fig. 3). The algorithm is defined below.

Elongation algorithm: (i) retrieve x,y coordinate (x_0, y_0) and angle of current head node, (ii) use biased random value function centered at current angle to find new angle θ, (iii) new x,y coordinates are defined by $(x_0 + 5, 5tan(\theta))$, (iv) check new x,y coordinates do not violate rules by running intersection algorithms, (v) if new coordinates violate rules, terminate the branch. Otherwise, add new head node to tracker.

Simulation results were filtered for simulations that were centered about the horizontal axis, and expressed approximately the same total width.

3 Results

After a continuous application of the uniaxial force to the mammary glands for two-weeks during puberty, carmine alum-stained whole mounts images of the mammary glands were used for morphometric analysis for CTL, TEN and CONTRA glands. Planar morphometric features where obtained for the glands including the length of the ductal network (measured from the nipple to the furthest branch, Fig. 2), the total area of the ductal network, the width of the ductal network (measured by the width of the smallest rectangle that encloses the ductal network, Fig. 2), number of branch bifurcations, number of side branches, thickest branch, thinnest branch, number of perimetral branches, orientation of the ducts (measured by the angular position of the ducts). The method for computing the morphometrics is described in the Materials and Methods.

We compared the values of the morphometric variables in TEN glands to CTL glands to determine if the applied uniaxial force affected mammary gland development. We also compared the values of the morphometric variables in CONTRA glands to CTL glands to determine if the contralateral forces resulting from the applied uniaxial force affected the ductal network formation. The mammary gland has a fairly negligible depth when compared to its length and width and is often considered to be a planar tissue. Therefore, studies in the literature on mammary gland morphometry are often done on planar images of the gland because the planar images provide adequate information without the additional cost that is usually associated with capturing volumetric images of the gland. A volumetric image refers to a visualization of a series of stacked two-dimensional (2D) images that allow for a volumetric representation of a three-dimensional (3D) object. Moreover, except for the area of the ducts, the other key morphometrics (i.e. ductal branch angles, ductal network length) used in this study are not expected to change in value albeit significantly if computed in 3D versus 2D.

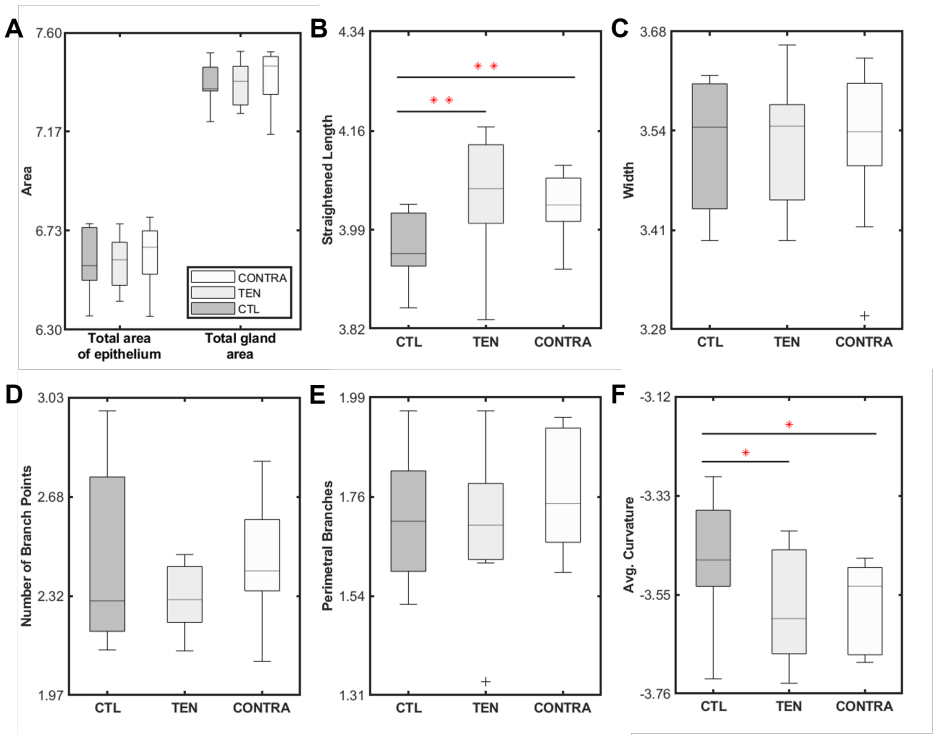

Fig 4. Morphometrics for CTL, TEN and CONTRA glands. All the y-axis is in log base 10. Red asterisk implies that there is a statistical significance difference between the two groups. * represents P <0.1, ** represents P < 0.05.

3.1 Application of uniaxial force did not affect the size of the ductal network and the entire mammary gland

The cross-sectional area of the ductal network and the whole mammary gland was used to estimate their size. The total cross-sectional area of the epithelium ductal network for TEN and CONTRA glands were compared to CTLs to determine if the uniaxial force altered the size of the epithelium ductal network. Similarly, the total area of the mammary gland was also compared to determine if uniaxial and contralateral force altered the overall size of the mammary gland. There was no statistical significant difference in the cross-sectional area for the mammary glands in TEN vs. CTL and in CONTRA vs. CTL (Mann-Whitney U-test, $P_{TEN/CTL} = 0.6045, P_{CONTRA/CTL} = 0.2400$, one-tailed). And no significant difference as well for the area of the epithelium ductal network (Mann Whitney U-test, $P_{TEN/CTL} = 0.6706, P_{CONTRA/CTL} = 0.3294$, one-tailed) (Fig. 4a)

3.2 Uniaxial force significantly increased the overall length of the epithelium ductal network for the TEN glands

The overall length of the epithelium ductal network, measured from the nipple to the farthest terminal end bud (TEB) was significantly longer in TEN and CONTRA compared to CTL glands (Fig. 4b, Mann Whitney U-test, $P_{TEN/CTL} = 0.02, P_{CONTRA/CTL} = 0.02$, one-tailed). Due to glands varying in curvature during development, the glands were straightened to avoid bias in measurements from the curvature before the length measurements were obtained. The length was obtained using ImageJ. This implies that the increased length for the ductal network in the TEN and CONTRA glands does not correspond to an increase in the cross-sectional area of the epithelium tissue and the total mammary gland. We found it interesting that the CONTRA glands had a median length that was larger than CTLs but smaller than the TEN glands (Fig. 4). Indicating that the increased length in epithelium ductal network may be varying with the type and magnitude of force applied. The uniaxial and contralateral forces did not alter the width of the epithelium ductal network. Which also indicates that the increased length of the ductal network observed in the TEN and CONTRA glands was not due to a reduction in the width of the mammary gland.

3.3 Uniaxial force minimized the variance in the number of ductal branch points for TEN and CONTRA glands

An important part of the ductal network are the branch bifurcations and side branches. Therefore, we counted the number of bifurcation points and side branching points in each of the images for TEN, CONTRA and CTL glands. We found that the uniaxial force made the glands to exhibit a smaller variance in the total number of branch bifurcations and side branches in TEN and CONTRA glands compared to CTLs. There was a significant increase in heterogeneity (variance) in the number of branches in CTL versus TEN glands (Levene's test; P=0.0006).

3.4 Uniaxial force altered the orientation of the ducts in the TEN and CONTRA glands

The organization/orientation of the individual ducts in the ductal network determines the spatial connectivity and overall shape of the ductal network. The orientation and spatial connectivity of the ducts affects the delivery of milk through the ducts to breastfeeding infants. Based on the physics of fluid flow, efficiency in milk delivery through the ducts would dependent on the diameter of the ducts,

the orientation of the ducts etc. Given the importance of ductal orientation, we sought to determine if the orientation of the ducts was affected by the uniaxial force. To determine the orientation of the ducts, we quantified the angular position of the pixels in the images for the ductal network. We computed the proportion of the ductal branches that where located in different angular position for the TEN, CONTRA and CTL ductal networks. The angular position was considered from between -90° to 90°. Fig. 5A-B shows the distribution of the ducts using histograms with bins of 60° width. The first bar in the histogram in Fig. 5A represents the ductal regions with angular position that were located between -90° and -30° for all the TEN versus CTL ductal network. The second bar is for the ductal regions with angular position represents the ductal regions with angular position that were located between -30° and 30°. Similarly, the third bar is for the ductal regions with angular position located between 30° and 90°. It can be observed that the ductal network for TEN had a higher proportion of ductal region located within $[-30^{\circ}, 30^{\circ}]$, whereas CONTRA had a higher proportion of ductal region located within $[-30^{\circ}, 90^{\circ}]$ compared to CTLs. On the other hand, CTLs had a a higher proportion of ductal region located within $[-90^{\circ}, -30^{\circ}]$ and $[30^{\circ}, 90^{\circ}]$ compared to those for TEN and a higher proportion in $[-90^{\circ}, -30^{\circ}]$ compared to CONTRA. Reducing the bin size of the histogram allowed us to determine smaller range of angles that contribute more to the observed changes in ductal network orientation between TEN versus CTL and CONTRA versus CTL.

We note here that if the bin size is very large (say 180°), then we will not be able to capture the differences between TEN, CONTRA and CTL ductal network. On the other hand, if the bin size is too small (say 1°), we will only learn that each ductal network is different. In order to select a good bin size for comparing the histograms, we computed the similarity in the distribution of the angular positions for TEN vs CTL and CONTRA vs CTL for different bin sizes. The similarity in the distribution of the angular positions for TEN vs CTL and CONTRA vs CTL was measured using the Wasserstein distance as described in the Materials and Methods. Wasserstein distance clearly captures the expected dynamics for how the similarity between the angle distributions would change with the histogram's bin size (Fig. 5C). A low values of Wassertein distance indicates a high similarity between the distributions and a high values of Wasserstein distance indicates a high degree of dissimilarity between the distribution (Fig. 5C). The rate of change in Wasserstein distance with respect to the bin size is linear. The graph of Wasserstein distance against bin size resembles a visual tool called elbow plot that is often used in cluster analysis and other machine learning algorithms to determine the optimal number of clusters. In particular, elbow plot identifies the point at which adding more clusters does not significantly improve the model performance, indicating a diminishing return. Using a similar idea as often used for elbow plots, we selected a bin size of 5° because it gives a value for

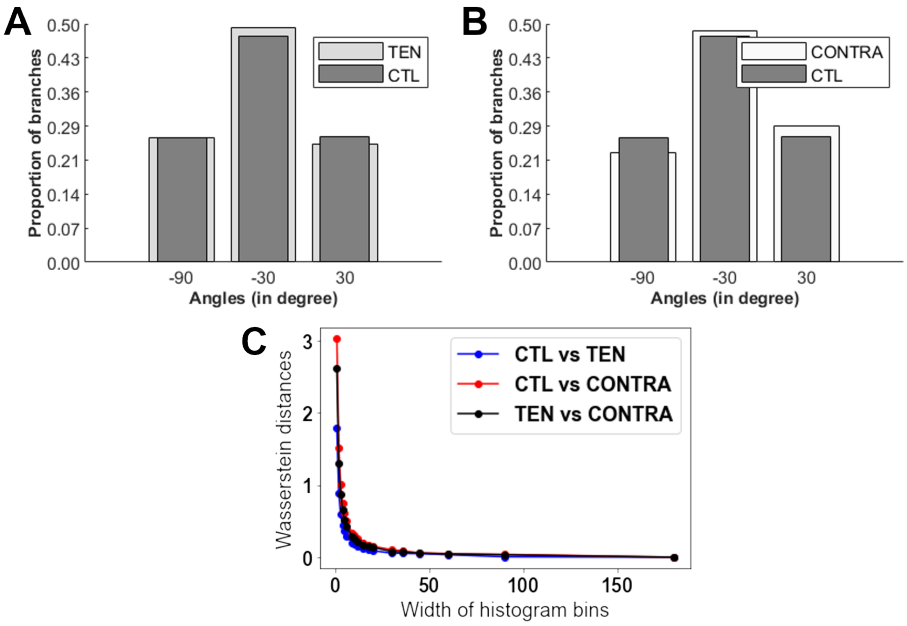

Fig 5. Comparison of the angular distribution of the bulk of the ductal network for TEN, CONTRA and CTL. Visual differences in angle distribution for TEN versus CTL and CONTRA versus CTL are shown in (A) and (B) respectively. Here the bin size is set at 60° angle. (C) The graph of Wasserstein distance against bin size shows how the degree of similarity in angle distribution between the different groups is dependent on the bin size.

Wasserstein distance close to the elbow of the graph in Fig. 5C.

Fig. 6 shows a visual comparison of the angle distribution for the ductal network for TEN versus CTL and CONTRA versus CTL using 5° angles for the bin size. Consistent with the angle distribution with 60° bin size, we see here that TEN glands consistently had higher proportion of ductal regions with smaller angular position (i.e. between $[-20^{\circ}, 35^{\circ}]$, Fig. 6A). Interesting, we see a different visual pattern evolve for the angle distribution for CONTRA versus CTL (Fig. 6B). Fig. 6B indicates that the higher proportion of angular regions in $[-30^{\circ}, 90^{\circ}]$ angles was due to a high proportion of ductal regions existing in the $[-5^{\circ}, 55^{\circ}]$ degree range. We recall here that the CONTRA glands experienced the uniaxial force on one side of its gland, that is on the side adjacent to the TEN gland. Interestingly, we see here that the higher proportion of smaller angles was only on one-side of the ductal netwok. Clearly, we see in Fig. 6A-B that the uniaxial force altered the orientation of the ducts in the TEN and CONTRA glands.

In addition to looking at bulk distribution of angles as shown in Fig. 6A-B, we also represented the distribution of angles for each individual ductal network. This was done to confirm consistency in the observed angle distribution at the bulk level with that exhibited by individual glands. For each 5° range of angles, we plot the proportion of each individual ductal gland in that range (Fig. 7). We

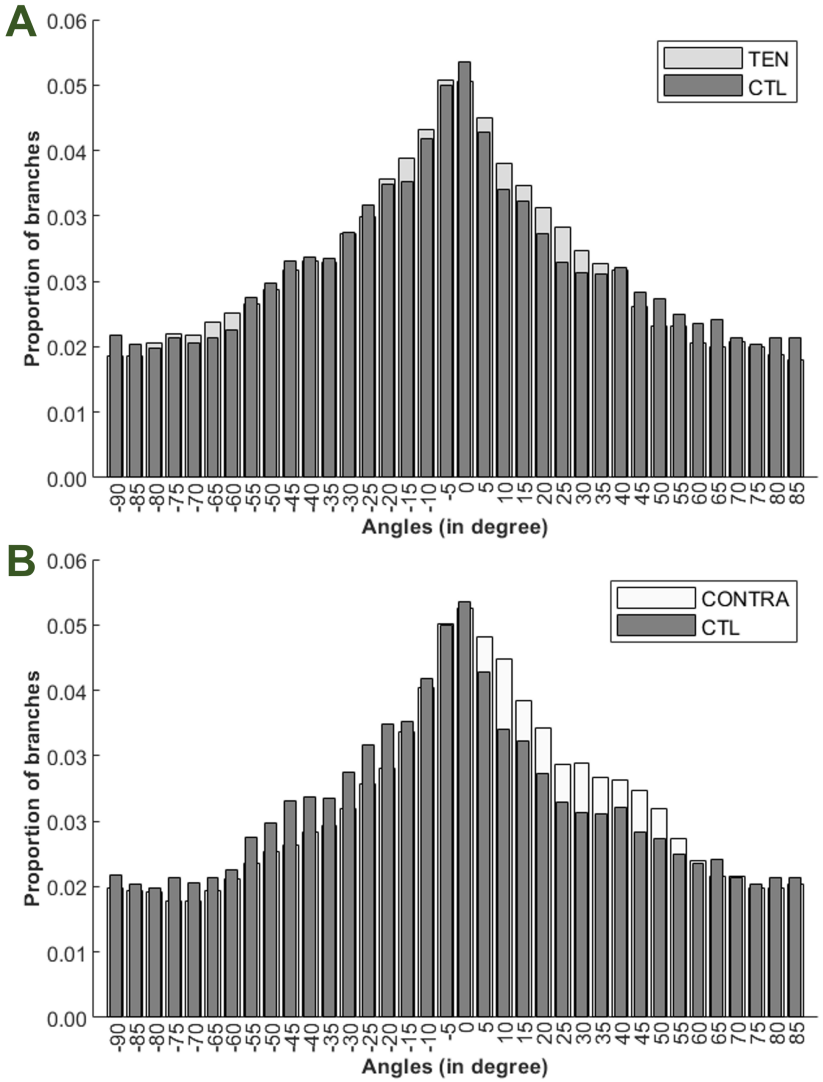

Fig 6. Angle distribution for the whole bulk of the ductal network. Here the bin size is set at 5° angle.

identified in Fig. 7 the range of angles that had consistently higher proportion of ductal regions for each of the individual glands. In particular, the TEN glands in general had a significantly higher proportion of ductal branches within the -15° to -11° range of angles. And the CTL glands had a significantly higher proportion of branches within 50° to 59° and 85° to 90° range of angles. CTL had a significantly higher proportion of ductal branching compared to CONTRA within -75° to -71° and -45° to -31°. In contrast, CONTRA had a significantly higher proportion of ductal branching compared to CTL in the following ranges: 10° to 14° and 20° to 29° We conclude here that the uniaxial force biased ductal orientation differently in CONTRA compared to the TEN glands. This implies that the direction of the applied force is important for controlling the orientation of the ducts. The orientation of daughter ducts is in general associated with the angle of branching from their parent

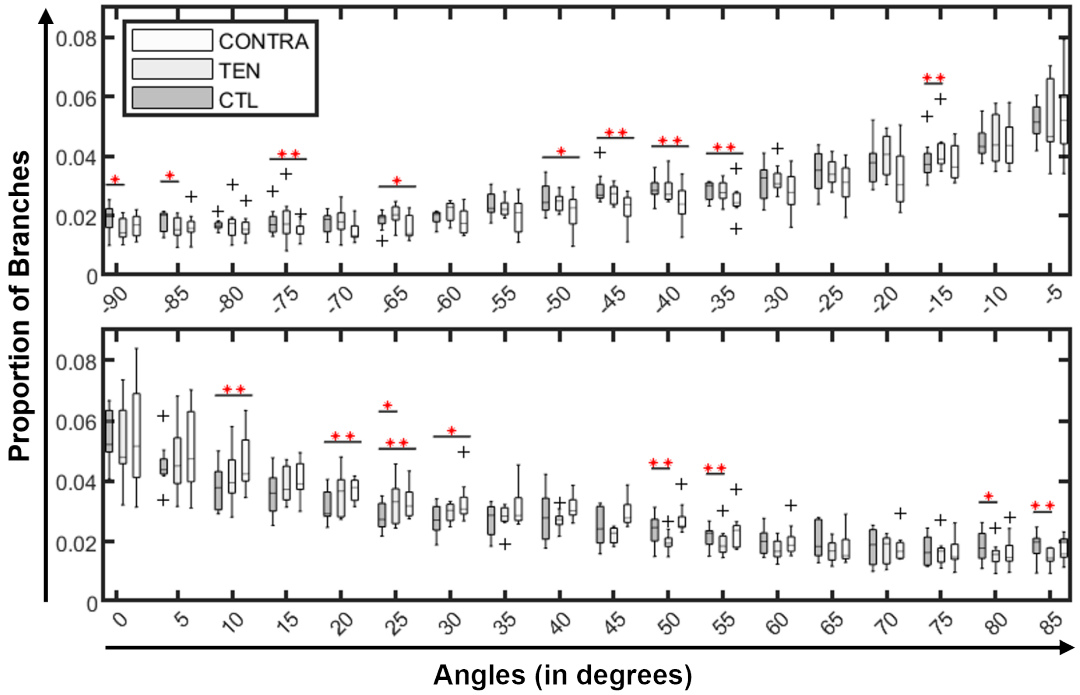

Fig 7. Visual differences in angle distribution for the individual ductal networks in the TEN versus CTL and CONTRA versus CTL are shown in (A) and (B) respectively. Here the bin size is set at 5° angle.

duct. We hypothesized that the increased length of the ductal network for the TEN and CONTRA glands may have resulted from changes in the orientation of the ducts. To test this hypothesis, we simulated ductal network formation using a biased annihilating random model and examined how variation in the orientation of ducts (modeled by varying the angle of branching of daughter ducts from their parent duct) affect the length of the ductal network. Description of the implementation of the is provided in the Materials and Methods.

3.5 Biased and annihilating random walk model predicts that the increased length of the ductal network in the TEN glands was due to the existence of smaller branch angle for ductal bifurcation in TEN compared to CTL gland

We simulated the biased and annihilating random walk model for 18 different instances, 9 for TEN and 9 for CTL. TEN glands were given a bias angle of 15° and -15° whereas CTL was given a bias angle of 50° and -50°. The simulations were run for 25 generations of ductal bifurcations, which appeared to be sufficient generations for multiple bifurcations and deaths. We calculated the length of the simulated

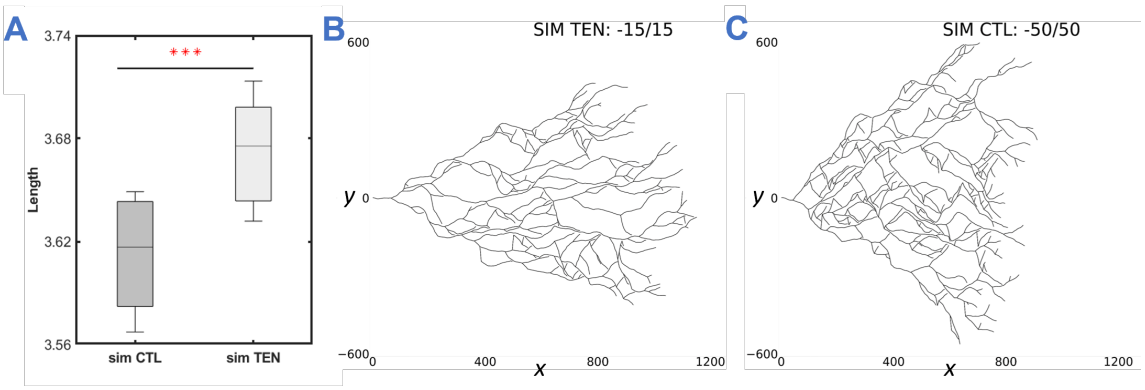

Fig 8. Random Walk Simulations. (A) shows the significant difference between the length of the simulated TEN versus CTL glands. (B & C) shows a sample simulated TEN and CTL gland respectively obtained after 25 generations of ductal bifurcations.*** denotes P< 0.005

ductal network and compared the results to our experimental data. The results from the simulation predicts that smaller angles of ductal bifurcation can significantly increase the length of the ductal network (Fig. 8).

We conducted further analysis for one-sided bias, where the simulation was giving only angle, rather than a positive and negative angle of the same distance from 0°. We used the upper and lower bounds of branching angles between CONTRA and CTL that were significant in the experimental data. We used $-75^{\circ}, -35^{\circ}, 10^{\circ}$, and 25°. We compared the one-sided angle simulations to two-sided angle simulations as well(supplemental). The results further confirm that small branching angles, one- or two-sided, result in significantly longer branching structures compared to branching structures that prefer to branch at larger branching angles. The results also show that two branching structures with a preference for small branching angles will not grow significantly longer than each other. The line between small and large branching angle appears to be at or above 35°.

4 Discussion

Identifying the mechanisms that regulate the orientation of the epithelium ductal branches is an important step towards unraveling the complex interactions that coordinate the formation of the mammary ductal network. In this study, we investigated if a uniaxial force applied during puberty can regulate the orientation of epithelium ducts in the ductal network. Using in-vivo experiments and computational modeling, we demonstrate that a uniaxial force applied to mice mammary glands for two-weeks during pubertal development increases the length of the whole ductal network and modifies the orientation of ducts in the ductal network. The cross-sectional area of the ductal network that

were exposed to the uniaxial and contralateral force (i.e. the TEN and CONTRA glands) were fairly similar to CTLs, which made us conclude that the increased length of the ductal network may not have corresponded to a change in size in the ductal network.

We introduced an approach that utilizes Wasserstein distance metrics to identify a good bin size for comparing the distributions of ductal angles in TEN and CONTRA glands to CTLs. The proportion of ducts at different angular regions in the ductal network for TEN and CONTRA was compared to CTLs, and we were able to determine how the orientation of ducts differ in TENs and CONTRAs versus CTLs. We hypothesized that the increased length in ductal network for the TEN and CONTRA glands may have been due to changes in orientation of the ducts compared to CTLs. Since the orientation of daughter ducts is in general associated with the angle of branching of daughter ducts from their parent duct, we tested this hypothesis by examine how variation in the ductal branch angles affect the length of ductal network. Using a biased branching and annihilating random walk model, we simulated ductal branching networks to determine how ductal branch angle influence the overall length of the ductal network. Results from the simulations predict that the increased length of the ductal network in the TEN glands may have been caused by alterations in branching angles. In particular, narrow ductal branch angles led to an increase in the length of the ductal network. Based on our findings, we concluded that the uniaxial force caused an increase in the length of the ductal network of the TEN glands by modifying the orientation of the ductal branches.

This study raises new questions concerning the mechanism by which the uniaxial force regulated the orientation of the ducts. That is, whether the changes in ductal orientation was orchestrated by purely physical interactions between the collagen fibers and ductal cells or if it was orchestrated by purely molecular factors, a combination of both or through entirely different mechanisms. Previous studies have demonstrated that the application of a uniaxial force to a tissue causes a uniaxial strain which leads to collagen reorganization in the direction of the uniaxial force. This is important because collagen organization alters the mechanical properties of the ECM, thereby affecting behavior such as cell adhesion, migration, and differentiation, which are key processes involved in branching morphogenesis. Also, traction forces exerted by ductal cells reorients and realigns collagen fibers in their preferred direction of migration or tension, facilitating cell movement through the ECM [24]. The reorganization of collagen fibers can in turn alter the stiffness of the ECM, thereby affecting cell behavior such as cell adhesion, migration, and differentiation. This creates a feedback loop where cell-generated forces remodel the ECM, which in turn influences cell behavior. Future work may focus on understanding how uniaxial force impact cell behavior during branching morphogenesis. This may yield new insights on how the tension force generated by interactions between the ductal cells and its surrounding ECM

affect the process of mammary branching morphogenesis.

Given that collagen fibers are a major component of the ECM mechanical properties and they provide contact guidance for cells, the changes in the ductal network resulting from the application of uniaxial and contralateral strain highlights the need to further investigate the role of collagen fiber orientation in the patterning of the shape of the ductal network in the mammary gland. The TEN and CONTRA glands had smaller variation in total number of branches within group compared to CTLs, which implies that the uniaxial force may have influenced the number of branch points and/or bifurcations in the ductal network.

In summary, findings from this study indicates that mechanical forces may regulate the orientation of ductal branches and the overall length of the ductal network. Improving our understanding of the mammary ductal network formation is important because the epithelium ductal network coordinates milk synthesis and secretion in lactating mammals for the breastfeeding of infants. The orientation/branching angles of the epithelium ducts determine the overall shape of the epithelium ductal network. An improved understanding of how mechanics impacts the formation of the epithelium ductal network is essential for understanding factors that may lead to developmental abnormalities. It may also yield insights into the formation of other branched organs and may potentially lead to the identification of novel ways to design artificial organs to combat diseases [43].

References

1. Bordeu I, Chatzeli L, Simons BD. Inflationary theory of branching morphogenesis in the mouse salivary gland. Nature communications. 2023;14(1):3422.

2. Deolmi M, Decarolis NM, Motta M, Makrinioti H, Fainardi V, Pisi G, et al. Early origins of chronic obstructive pulmonary disease: prenatal and early life risk factors. International Journal of Environmental Research and Public Health. 2023;20(3):2294.

3. Pederiva F, Rothenberg SS, Hall N, Ijsselstijn H, Wong KK, von der Thüsen J, et al. Congenital lung malformations. Nature Reviews Disease Primers. 2023;9(1):60.

4. Sharma S, Sureka B, Yadav T, Panda A, Khera PS. The Varieties of Ignorance: Imaging of Congenital Variants of Pancreas and Its Ductal System—A Pictorial Review. Indian Journal of Radiology and Imaging. 2024;34(02):324–331.

5. Woods JC, Schittny JC. Lung structure at preterm and term birth. Fetal lung development-clinical correlates & future technologies Cambridge University Press, New York. 2016; p. 126–140.

6. Liljekvist MS, Foghsgaard J, Howitz MF. Sialendoscopy for pediatric salivary gland disorders: a study of safety and effect. European Archives of Oto-Rhino-Laryngology. 2023;280(4):1927–1937.

7. Menshykau D, Michos O, Lang C, Conrad L, McMahon AP, Iber D. Image-based modeling of kidney branching morphogenesis reveals GDNF-RET based Turing-type mechanism and pattern-modulating WNT11 feedback. Nature communications. 2019;10(1):239.

8. George UZ, Lubkin SR. Tissue geometry may govern lung branching mode selection. Journal of theoretical biology. 2018;442:22–30.

9. Uçar MC, Hannezo E, Tiilikainen E, Liaqat I, Jakobsson E, Nurmi H, et al. Self-organized and directed branching results in optimal coverage in developing dermal lymphatic networks. Nature Communications. 2023;14(1):5878.

10. Richert MM, Schwertfeger KL, Ryder JW, Anderson SM. An atlas of mouse mammary gland development. Journal of mammary gland biology and neoplasia. 2000;5:227–241.

11. Sternlicht MD. Key stages in mammary gland development: the cues that regulate ductal branching morphogenesis. Breast Cancer Research. 2005;8(1):1–11.

12. Myllymäki SM, Mikkola ML. Inductive signals in branching morphogenesis–lessons from mammary and salivary glands. Current Opinion in Cell Biology. 2019;61:72–78.

13. Lanigan F, O'connor D, Martin F, Gallagher W. Common Molecular Mechanisms of Mammary Gland Development and Breast Cancer: Molecular links between mammary gland development and breast cancer. Cellular and Molecular Life Sciences. 2007;64:3159–3184.

14. Biswas SK, Banerjee S, Baker GW, Kuo CY, Chowdhury I. The mammary gland: basic structure and molecular signaling during development. International Journal of Molecular Sciences. 2022;23(7):3883.

15. Mertelmeyer S, Weider M, Baroti T, Reiprich S, Fröb F, Stolt CC, et al. The transcription factor Sox10 is an essential determinant of branching morphogenesis and involution in the mouse mammary gland. Scientific reports. 2020;10(1):17807.

16. Kessenbrock K, Smith P, Steenbeek SC, Pervolarakis N, Kumar R, Minami Y, et al. Diverse regulation of mammary epithelial growth and branching morphogenesis through noncanonical Wnt signaling. Proceedings of the National Academy of Sciences. 2017;114(12):3121–3126.

17. Sternlicht MD. Key stages in mammary gland development: the cues that regulate ductal branching morphogenesis. Breast Cancer Research. 2005;8:1–11.

18. Sternlicht MD, Kouros-Mehr H, Lu P, Werb Z. Hormonal and local control of mammary branching morphogenesis. Differentiation. 2006;74(7):365–381.

19. Kouros-Mehr H, Werb Z. Candidate regulators of mammary branching morphogenesis identified by genome-wide transcript analysis. Developmental dynamics: an official publication of the American Association of Anatomists. 2006;235(12):3404–3412.

20. Chatterjee SJ, Halaoui R, Deagle RC, Rejon C, McCaffrey L. Numb regulates cell tension required for mammary duct elongation. Biology Open. 2019;8(5):bio042341.

21. Lan Q, Trela E, Lindström R, Satta JP, Kaczyńska B, Christensen MM, et al. Mesenchyme instructs growth while epithelium directs branching in the mouse mammary gland. Elife. 2024;13:e93326.

22. Satta JP, Lan Q, Taketo MM, Mikkola ML. Stabilization of epithelial β-catenin compromises mammary cell fate acquisition and branching morphogenesis. Journal of Investigative Dermatology. 2024;144(6):1223–1237.

23. Nerger BA, Jaslove JM, Elashal HE, Mao S, Košmrlj A, Link AJ, et al. Local accumulation of extracellular matrix regulates global morphogenetic patterning in the developing mammary gland. Current Biology. 2021;31(9):1903–1917.

24. Buchmann B, Engelbrecht L, Fernandez P, Hutterer F, Raich M, Scheel C, et al. Mechanical plasticity of collagen directs branch elongation in human mammary gland organoids. Nature Communications. 2021;12(1):2759.

25. Hennighausen L, Robinson GW. Information networks in the mammary gland. Nature reviews Molecular cell biology. 2005;6(9):715–725.

26. Bussard KM, Smith GH, et al. The mammary gland microenvironment directs progenitor cell fate in vivo. International journal of cell biology. 2011;2011.

27. Wang F, Gao S, Chen F, Fu Z, Yin H, Lu X, et al. Mammary fat of breast cancer: gene expression profiling and functional characterization. PLoS One. 2014;9(10):e109742.

28. de Jonge N, Kanters FM, Baaijens FP, Bouten CV. Strain-induced collagen organization at the micro-level in fibrin-based engineered tissue constructs. Annals of biomedical engineering. 2013;41:763–774.

29. Walma DAC, Yamada KM. The extracellular matrix in development. Development. 2020;147(10):dev175596.

30. Nelson CM. Mechanical control of cell differentiation: Insights from the early embryo. Annual Review of Biomedical Engineering. 2022;24:307–322.

31. Kim HY, Nelson CM. Extracellular matrix and cytoskeletal dynamics during branching morphogenesis. Organogenesis. 2012;8(2):56–64.

32. Mary H, Brouhard G. Kappa (κ): analysis of curvature in biological image data using B-splines. BioRxiv, 852772; 2019.

33. Schindelin J, Arganda-Carreras I, Frise E, Kaynig V, Longair M, Pietzsch T, et al. Fiji: an open-source platform for biological-image analysis. Nature methods. 2012;9(7):676–682.

34. Schneider CA, Rasband WS, Eliceiri KW. NIH Image to ImageJ: 25 years of image analysis. Nature methods. 2012;9(7):671–675.

35. Rezakhaniha R, Agianniotis A, Schrauwen JTC, Griffa A, Sage D, Bouten Cv, et al. Experimental investigation of collagen waviness and orientation in the arterial adventitia using confocal laser scanning microscopy. Biomechanics and modeling in mechanobiology. 2012;11:461–473.

36. Püspöki Z, Storath M, Sage D, Unser M. Transforms and operators for directional bioimage analysis: a survey. Focus on bio-image informatics. 2016; p. 69–93.

37. Fonck E, Feigl GG, Fasel J, Sage D, Unser M, Rufenacht DA, et al. Effect of aging on elastin functionality in human cerebral arteries. Stroke. 2009;40(7):2552–2556.

38. Thorpe M. Introduction to optimal transport. Lecture Notes. 2019;3.

39. Zhou R, Gueaieb W, Spinello D. A Model-Free Kullback–Leibler Divergence Filter for Anomaly Detection in Noisy Data Series. Journal of Dynamic Systems, Measurement, and Control. 2023;145(2):024501.

40. Berg HC. Random walks in biology. Princeton University Press; 1993.

41. Hannezo E, Scheele CL, Moad M, Drogo N, Heer R, Sampogna RV, et al. A unifying theory of branching morphogenesis. Cell. 2017;171(1):242–255.

42. Hannezo E, Scheele CL. A Guide Toward Multi-scale and Quantitative Branching Analysis in the Mammary Gland. In: Cell Migration in Three Dimensions. Springer; 2023. p. 183–205.

43. Patel VN, Rebustini IT, Hoffman MP. Salivary gland branching morphogenesis. Differentiation. 2006;74(7):349–364.